On pressure-driven Poiseuille flow with non-monotonic rheology

L. Talon, D. Salin

On pressure-driven Poiseuille flow with nonmonotonic rheology

L. Talon* and D. Salin†
Université Paris-Saclay, CNRS, FAST, 91405, Orsay, France.

Shear thickening fluids are liquids that stiffen as the applied stress increases. If many of these types of fluids follow a monotonic rheological curve, some experimental and numerical studies suggest that certain fluids, like cornstarch, may exhibit a non-monotonic, S-shaped rheology. Such non-monotonic behaviour has however proved very difficult to observe experimentally in classical rheometer. To explain such difficulties, the possible presence of vorticity banding in the rheometer has been considered. To prevent such instabilities, we use a capillary rheometer, which is a cylindrical tube, measuring the flow rate versus the applied pressure drop. With this set up, we indeed observe a non-monotonic behavior: the flow rate increases monotonically at low pressure drops up to a maximum, after which it abruptly decreases to an almost constant flow rate regardless of further increases in pressure drop. This maximum-jump-plateau behavior occurs over a wide range of concentrations and is reproducible without hysteresis, which is in agreement with an S-shaped rheology. However, the obtained flow versus pressure difference function $Q(\Delta P)$ does not agree with the classical Wyart-Cates rheological model, which predicts an S-shaped non-monotonic function, but with neither a jump nor a plateau. To understand this jump-plateau behaviour, we remark that any rheological model would establish a relationship between the flow rate and the local pressure gradient, but not the total pressure drop. We thus discuss and analyze the implications of having an S-shaped non-monotonic flow rate-pressure gradient in Poiseuille flow. In particular, we discuss the possibility of a non-uniform pressure gradient in the direction of the flow, i.e. a kind of streamwise banding. The key issue is then the selection of the gradient pressure distribution along the tube. One solution could arise from an analogy of this problem with the spinodal decomposition. It, however, leads to an increase in flow rate with $\partial_x P$ up to a plateau between two values of $\partial_x P$ as determined by the Maxwell construction. To account for the bump-jump behavior, we have implemented a simple dynamical stochastic version of the Wyart-Cates model, where the thickening occurs with a characteristic time. As a result, with increasing the total pressure drop, the flow rate increases monotonically up to a maximum value. Beyond this point, the flow rate drops abruptly to a lower value, forming a slowly decreasing plateau. This behavior is likely to account for the maximum-jump-plateau observed in the experiments. We also show that in such a system, the final state is quite sensitive to the initial state of the fluid, especially its homogeneity. Our results then demonstrate that the mere presence of a non-monotonic rheological curve is sufficient to predict the occurrence of stress banding in the streamwise direction and a plateau flow rate, even if the suspension remains homogeneous.

I. INTRODUCTION

Newtonian liquids, such as water, glycerin, or honey, are characterized by a linear relationship between shear stress and shear rate, which allows for the definition of a constant viscosity, η. In contrast, many complex fluids, such as particulate suspensions, surfactant solutions, or cornstarch, are following the so-called generalized Newtonian rheology, where the viscosity is a function of the shear-rate (or the shear-stress). When dealing with such fluids, applying a shear rate results in a specific shear stress. It then leads to the determination of the relationship between the shear stress and the shear rate, $\tau(\dot\gamma)$, known as the flow curve. This also allows to define a viscosity function of the shear rate: $\tau(\dot\gamma) = \eta(\dot\gamma)\dot\gamma$. Depending on whether the viscosity is increasing or decreasing with $\dot\gamma$, characterized shear thinning or shear thickening fluids respectively. Similarly, by imposing the shear stress τ, we can define a relationship between the shear rate and the shear stress $\dot\gamma(\tau)$, and a viscosity dependent on shear stress $\eta(\tau)$. Shear thickening fluids, where viscosity increases with shear stress, have attracted a lot of attention due to their remarkable properties. In particular, some fluids exhibit a very abrupt increase in viscosity for a given shear stress. This property is usually referred to as discontinuous shear thickening (DST) [1–3], in contrast to the classical continuous shear thickening (CST) [1, 4]. Many different fluids displays DST, but one very famous example is the cornstarch suspension that allows to run on its surface [4]. The physical origin of DST has been the subject of many different studies [2–5]. While the dilatancy [4, 6, 7] or the hydroclustering [8] has been invoked, the most recent convincing explanation invokes the combination of repulsive interactions and frictional contact between the particles [3, 9–11]. Because suspensions with frictional and frictionless (lubricated) contacts have different viscosity branches [12], repulsive forces control the transition from one branch to the other. When the stress is low, the contacts are mainly frictionless, but when the stress exceeds the repulsive force, it allows frictional contacts between the particles, leading to a drastic increase in viscosity. This is, for instance, the essence of

* laurent.talon@universite-paris-saclay.fr
† salin@fast.u-psud.fr

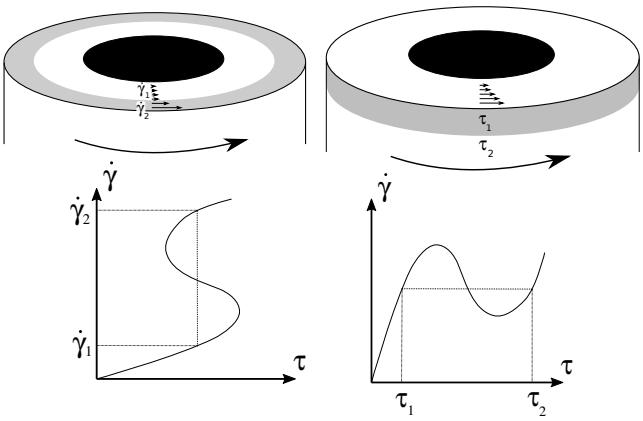

Figure 1. Sketch of shear banding (top left) and vorticity banding (top right) as proposed by [18]. For shear banding, the rheological curve $\tau(\dot{\gamma})$) is single valued but non-monotonic (bottom left). For vortex banding it is the $\dot{\gamma}(\tau)$ curve which is single valued and non-monotonic (bottom right).

the model proposed by Wyart and Cates [10] that will be discussed later.

Even more interesting is the prediction that the flow curve might display an S-shaped curve, where $d\dot{\gamma}(\tau)/d\tau < 0$ for a range of stresses and concentrations, distinguishing continuous shear thickening (CST) from discontinuous shear thickening (DST). This type of curve is interesting because while the curve $\dot{\gamma}(\tau)$ is single-valued, imposing the shear rate $\dot{\gamma}$ leads to three possible shear stresses. Moreover, in such conditions, homogeneous flow is expected to be mechanically unstable [3, 13]. This is the reason why the S-shaped flow curve has been mainly reported theoretically and numerically [14, 15], but experimental evidences are quite rare [13, 16].

One particular particular mechanical instability is the potential occurrence of "vorticity banding," [17] where the regions of the fluids pile up (on the right of Figure 1) along the vorticity direction in the rheometer, i.e. perpendicular to the flow direction (vertical in the sketch). In each layer, the shear rate is the same but with different shear stresses. This kind of banding needs to be distinguished from the shear (or gradient) banding that occurs in S-shaped shear thinning fluids [18, 19], where a specific stress can result in different shear rates. Along the shear direction, i.e. radial, the fluid segregates between high shear rate and low shear rate regions (left of Figure 1). It should also be noted that shear banding can be caused by mechanisms other than rheology. For example, shear banding has been reported due to particle migration inducing density inhomogeneities. This particle migration can be due to shear induced migration or due to gravitational effects . This density inhomogeneity may thus responsible for an apparent nonlinear rheology (shear-thining, shear-thickening, yield stress, etc.) in the rheometer (see [1, 2, 20]).

Vorticity banding has been analyzed numerically and experimentally by [18, 21]. It has been reported that such banded flows are inherently unstable, leading to time-dependent flows characterized by fluctuating shear stresses and rates. These unsteady flows range from relatively simple oscillations to fully developed chaos. Shear-band-like features may or may not remain stable. Therefore, it is experimentally rather difficult to ascertain the S-shaped rheological curve [16, 22–24].

In order to avoid vorticity banding and instabilities that occur in classical viscometer (Figure 1, right), we choose to use a Poiseuille flow configuration, the capillary rheometer as proposed for instance, by [25]. The set-up consists of a cylindrical tube with a circular cross-section of radius R and length L, and measuring the volume flow rate Q versus the pressure drop ΔP across the length. The axisymmetry of the cylindrical geometry is likely to suppress the formation of vorticity banding. The so-called Weißenberg-Rabinowitsch (WR) equation [26] leads to the relationship between the shear rate $\dot{\gamma}_w$ and the shear stress at the wall ($\tau_w = \Delta P R/(2L)$):

$$\dot{\gamma}_w(\tau_w) = \frac{Q(\tau_w)}{\pi R^3}(3+n) \text{ with } n = \frac{dLogQ(\tau_w)}{dLog(\tau_w),} \quad (1)$$

leading to the flow curve $\dot{\gamma}(\tau)$. Newtonian fluids correspond to $n = 1$ leading to the Weißenberg-Rabinowitsch correction [26] which should be only used for the term $(3 + n)/4$. Several comments should be made about this expression. First, its derivation is based on the lubrication approximation, which assumes that the local pressure gradient, $G = \partial_x P$ is aligned with the streamwise direction, is constant, and equals $G = \Delta P/L$. It is also worth noting that discarding the n term, the shear rate is almost proportional to the flow rate. It is thus expected that the curve $Q(\Delta P)$ exhibits the same variations as $\dot{\gamma}(\tau)$. In particular, if $\dot{\gamma}(\tau)$ is non-monotonic, then the relationship between flow rate and pressure drop, $Q(\Delta P)$ will also not be monotonic.

The purpose of this paper is to evaluate the use of a Poiseuille flow configuration to track the S-shaped curve of the flow. In particular, we will show that if the flow rate-pressure gradient is non-monotonic, one can expect a different type of banding in the flow direction. We can note several works on suspension flows in Poiseuille configuration. Isa *et al.* [27] performed concentrated colloidal suspension flow in microchannel. For small enough channel gap, they observed fluctuating flow rate and velocity profile, which where confirmed by numerical simulations [28]. Since our gap is relatively larger, we didn't observe such velocity fluctuations in the present case. In a very recent experiment, Bouguoin *et al.* [29] analyzed a gravity-driven flow of cornstarch in an inclined tube. In particular, they observe the presence of a "frictional soliton" propagating upstream caused by the density change (dilation) of the trapped state. Since the configuration is quite close to the present study, a more detailed discussion will be given in the Discussion/Conclusions section.

The article is structured as follows. First, we present the rheological model of Wyart and Cates [10] which

enables the determination of the relationship between flow rate and the overall applied pressure. Then, we will present experimental results of cornstarch suspension in Poiseuille flow in a cylindrical tube. We will demonstrate that the flow curve - pressure drop is non-monotonic. However, it does not align with the predictions of the rheological model by Wyart and Cates, as it displays a bump followed by a prolonged plateau. In the following section, we will present a potential solution based on minimizing the energy of Poiseuille flow, which enables the prediction of a plateau but not a non-monotonic behavior. We will then present a dynamic toy model that allows us to reproduce the plateau and the non-monotonic bump. Finally, we will discuss our results and draw conclusions.

II. WYART AND CATES RHEOLOGICAL MODEL

In this section, we briefly recall the shear thickening rheology proposed by Wyart and Cates [10] to describe the shear thickening behavior and the S-shaped flow curve. It is based on two types of particle interactions: frictionless (lubricated) contacts and frictional contacts. Frictionless contacts occur when the applied stress is below the repulsive force between the particles, while frictional contacts occur when the applied stress exceeds it. The fraction of frictional contact, f is expected to increase with the stress $f = 1 - \exp(-\tau/\tau_*)$, where τ_* is a characteristic stress value. The main idea is that the increase in the fraction of frictional contacts decreases the volume fraction ϕ at which the viscosity diverges. It results that if ϕ is held constant, the viscosity $\eta(f)$ increases with f and consequently, with the applied stress. Without going into the details, they proposed a relationship in the form:

$$\eta(f) = \left[f\eta_r^{-1/\alpha} + (1-f)\eta_s^{-1/\alpha} \right]^{-\alpha}, \qquad (2)$$

where $\alpha = 2$ and η_s and η_r are respectively the viscosity of the suspension when there are only frictionless contacts ($f = 0$) and only frictional contact ($f = 1$). η_r and η_s depend on the volume fraction ϕ according to $\eta_{r,s} = \eta_0(\phi_{r,s} - \phi)^{-2}$, where $\phi_{r,s}$ are the volume fractions of viscosity divergence for frictional and frictionless modes respectively (see [12]). It is worth mentioning that since we are working at a fixed volume fraction, one could also simply use η_r and η_s as parameters.

A very interesting feature of this model is that it predicts non-monotonous rheology for some parameter sets. Figure 2 [left] displays the flow curve with the parameters found in [16]. It exhibits different behaviors. As expected, for low stress $\tau \lesssim \tau_*$, the rheology is Newtonian. A change in viscosity occurs when $\tau \simeq \tau_*$. For small ϕ, the change is relatively smooth, indicating a CST. For higher volume fraction $\phi \simeq 0.40$, the increase in viscosity is much sharper, which is a characteristic of DST. For $\phi \gtrsim 0.41$, the flow curve displays an S-shape, with Newtonian behavior at low and high shear stress. For a higher volume fraction, when the viscosity of frictional contact becomes infinite $\phi > 0.43$, the flow curve drops to zero without increasing again at high τ. Interestingly, this rheological model has been successfully used to fit numerical data [30], or experimental data [16], but with a different dependence of the number of frictional contacts with stress: $f = exp(-\tau_*/\tau)$ (see [9, 31]).

From the curve $\dot{\gamma}(\tau) = \tau/\eta(\tau)$, obtained with this rheological model, it is then possible to determine the total flow rate as a function of the applied pressure drop using the Weißenberg-Rabinowitsch formulation [26]:

$$Q(\Delta P) = \pi R^3 \frac{1}{\tau_w^3} \int_0^{\tau_w} \dot{\gamma}(\tau)\tau^2 d\tau. \qquad (3)$$

Note that eq. (1) is obtained by deriving eq. (3). The flow rate Q as a function of the pressure drop is plotted in Figure 2 [Right], using the same parameters as the ones in the left figure. As mentioned above, the flow rate $Q(\Delta P)$ follows the same trend as $\dot{\gamma}(\tau)$. One should, therefore, expect a non-monotonic variation in the flow rate with the pressure drop when the rheology exhibits an S-shaped flow curve.

III. EXPERIMENT

We use density-matched solvent and particles to eliminate shear thinning effects and migration [20]. We use cornstarch particles (Sigma-Aldrich, CAS 9005-25-8 S426), in a density-matched solvent composed of a mixture of 40 % water, 60 % glycerin, and cesium chloride ($CsCl$) [24]. The concentration of $CsCl$ is adjusted using a densimeter (Anton Paar DMA 35) to achieve density matching with the cornstarch. This is achieved for a concentration close to 55 $wt\%$ leading to a solvent of density, $\rho = 1650\ Kgm^{-3}$ and a viscosity 10.8 $mPa.s$; note that because we use matched density suspensions, the weight and volume concentrations are identical. The cornstarch concentration, ϕ, varies in the range 36 % to 42 %. The solutions are prepared the day before and mixed again for one hour before use. The cylindrical tube is $L = 100\ mm$ long with a radius of $R = 1.2\ mm$. The differential pressure with the atmospheric pressure is measured at the inlet with a 1 Pa accuracy. The outlet is at atmospheric pressure, allowing for the determination of the pressure drop ΔP across the cylindrical tube. The inlet pressure is increased step by step using a flow controller (ELVEFLOW OB1 MK4). At each step, the outlet flow rate converges after a few seconds. The recording time is typically 2 min. The mass flow rate Q_m is measured using a balance (accuracy $0.1mg$). The overall accuracy is mainly due to the size of the drops forming at the outlet (typical weight of 10 mg). The corresponding volume flow rate Q involved in eq. (1) is $Q = Q_m/\rho$. The left of Figure 3

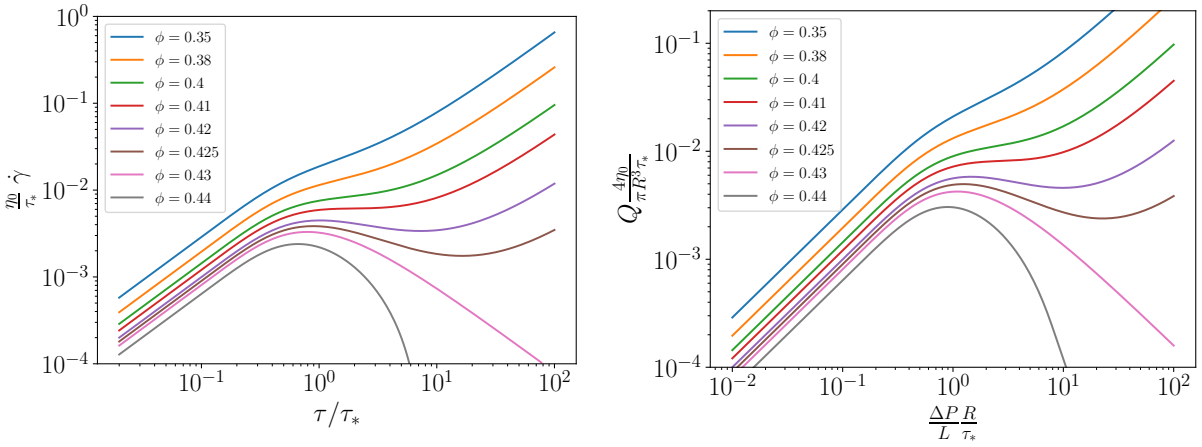

Figure 2.

Left: Shear rate as a function of the shear stress for different particle volume fraction following the Wyart and Cates model with Mari *et al.*[9] function of contacts $f = \exp(-\tau_*/\tau)$. Here, we use $\phi_r = 0.43$ and $\phi_s = 0.52$. Right: Corresponding flow rate as function of the pressure drop using the RW equation eq. (3).

displays a zoomed-in view of the relationship between the flow rate, Q, and the pressure drop, ΔP across the tube for a $\Phi = 39$ % suspension. The plot on the right shows the deduced relationship between shear rate and shear stress using eq. (1). The logarithmic derivative of the flow rate, n, involved in eq. (1)) is determined through a numerical fit to the data. The left side of Figure 4 shows a Log-Log plot of the flow curve, $\dot{\gamma}(\tau)$, for a series of concentrations ranging from $\phi = 36\%$ at the top to $\phi = 42\%$ at the bottom. For all these concentrations, except at 36%, increasing the shear stress τ from low values, the shear rate ($\dot{\gamma}$) increases monotonically up to a maximum, at which point it abruptly drops to a value typically half of its maximum value. For much larger shear stress, the shear rate value remains almost the same, forming a plateau. To test the reproducibility of the maximum-jump-plateau behavior, we investigate its vicinity by successively increasing and decreasing the pressure drop. The right-hand side of Figure 4 shows the robustness of this behavior. In Appendix A we report a complementary measurement obtained by measuring the pressure drop at a given flow rate, $\Delta P(Q)$, using our capillary rheometer. The green square data in Figure 11, is a plot of ΔP versus the controlled flow rate Q. Increasing the flow rate from low values, the pressure drop, i.e. τ increases monotonously up to a flow rate value at which the pressure increases drastically to the maximum measurable with our device, while the flow rate remains constant. In order to reduce the pressure, we need to decrease the flow rate. Therefore, in this flow rate-controlled experiment, we observe a $\Delta P(Q)$ curve that is monotonically increasing up to a maximum flow rate Q_M at which the pressure increases almost infinitely. This monotonous trend is evidently in line with the values acquired in the experiments utilizing the pressure-controlled device ($Q(\tau)$) up to the maximum flow rate. Hence, with a controlled flow rate, we can only access the continuous shear thickening part of the curve and are unable to access the jump-plateau part of the flow curve. Therefore, this jump-plateau behavior is likely specific to our pressure-controlled procedure and has not, to our knowledge, been previously reported in classical rheometry.

IV. SOLUTIONS OF NON-MONOTONIC POISEUILLE FLOW

Our experimental data do not correspond to any rheological curve reported in the literature (experimental or numerical) when assuming the Weißenberg-Rabinowitsch equation. [32] Besides, the WR equation is based on the reasonable assumptions of lubrication, which include stationary, non-inertial, and parallel flow. In the following, we will try to understand the possible origin of discrepancies in the experimental data, assuming that both the rheological model and the lubrication approximation are valid. There is indeed a major caveat in the RW equation eq. (1) which is the assumption that the stress at the wall is homogeneous along the flow direction. Indeed, if the lubrication approximation leads to a uniform pressure gradient in the transverse direction, this is not necessarily true along the flow $x-$ direction.

The lubrication approach leads to an expression of the local flow rate as a function of the local pressure gradient $G = \partial_x P$:

$$Q = -q(|G(x)|)\frac{G(x)}{|G(x)|}, \tag{4}$$

where $q(y)$ is a function given by eq (3) and that may be non-monotonic.

A solution of the problem consists in the determination of the pressure distribution $P(x)$ and the total flow

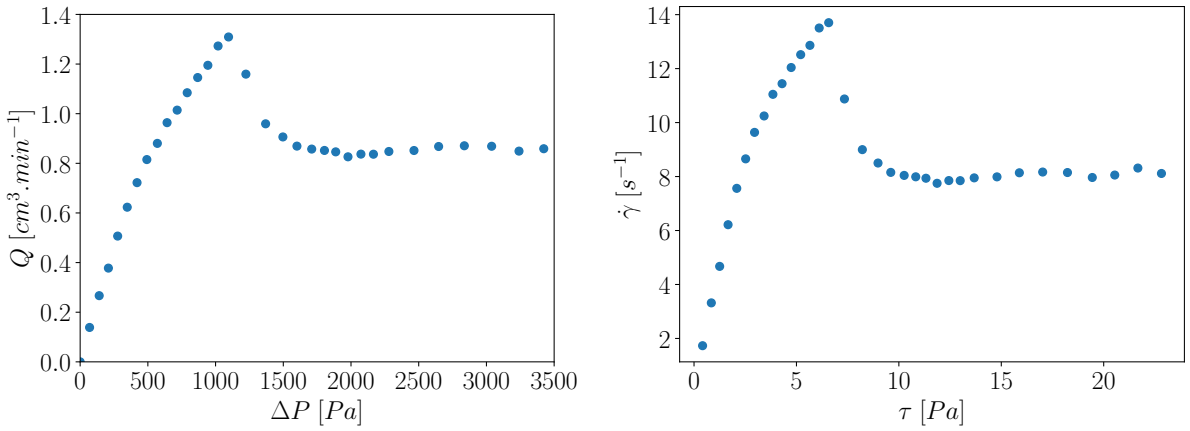

Figure 3. Experimental results for cornstarch with a concentration $\phi = 39$ %. Left : Flow rate (Q) versus pressure drop (ΔP). Right: Corresponding shear rate $\dot{\gamma}$ versus shear stress τ using eq. 1

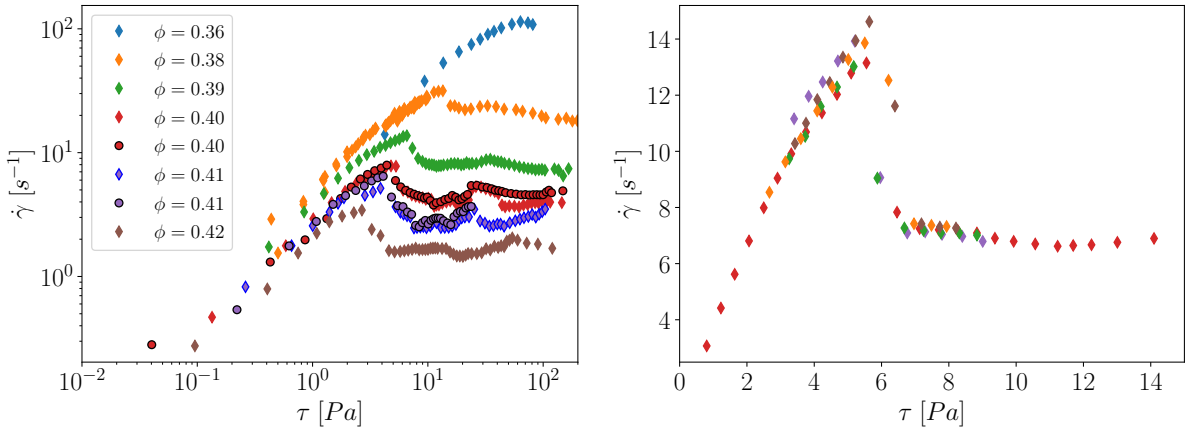

Figure 4. Left: Log-Log plot of the shear rate, $\dot{\gamma}$ (s^{-1}), versus shear stress $\tau(Pa)$ for concentrations varying from top to bottom, ranging from $\phi = 36$ % to $\phi = 42$ % . Right: Zoom around the maximum-jump zone for $\phi = 40$ %. The red circles correspond to a step-by-step increase in the pressure drop over a wide range of values, as shown in the left figure; the blue and green circles represent two successive increases followed by a decrease around the maximum jump; the different symbols in the same color correspond to the increase and the decrease.

rate Q, satisfying eq. (4), the conservation of mass, and the imposed pressure at the boundary. For an S-shaped rheological curve, the solution is not uniquely defined because for a range of ΔP, a given Q corresponds to three admissible pressure gradients. In contrast to the Newtonian case, there are therefore many admissible pressure distributions, but also flow rate values that are solutions of eq. (4). Many solutions might present different pressure gradients as shown in Fig 5 in the form of streamwise bands. The question that arises at this point is which solution the system selects.

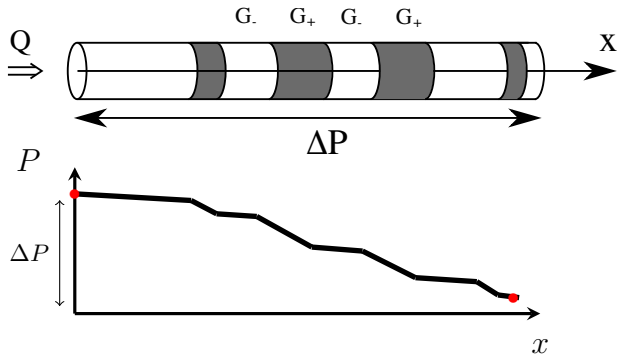

Figure 5. Sketch of a plausible streamwise banding configuration in the flow direction. While the total pressure drop is imposed as ΔP, the pressure gradient can be inhomogeneous, dividing into regions of high viscosity (G_+) and low viscosity (G_-).

A. Functional minimization

The first natural idea to determine a solution is the analogy with thermodynamics, specifically the spinodal decomposition, where the derivative of free energy

(chemical potential) is a non-monotonic function of the concentration of a species [33]. In this framework, the minimization of the total free energy leads to a phase transition, where some regions are in one phase while other regions are in another phase. In the present case, we cannot really define a free energy; however, we can use a variational principle. Since the work of Korteweg [34], it is known that the solution of Stokes' equations minimizes the viscous dissipation, and this has been generalized to non-Newtonian fluids by Bird [35]. A similar principle can be generalized to the non-linear Darcy's equation, such as the Poiseuille flow eq. (4) (see [36]), which can be expressed as follows: If the function $q(y)$ is monotonically increasing (i.e $q'(y) > 0$) then the solution of eq. (4) with an imposed pressure drop ΔP, is also the minimum of the function:

$$\{P\} = \arg\min_{\{P\}} \int_0^L \varphi(|G(x)|)dx, \tag{5}$$

with

$$\varphi(|G|) = \int_0^{|G|} q(y)dy. \tag{6}$$

This principle is valid when $q(y)$ is increasing, i.e $\varphi(y)$ is convex. For a non-monotonic function $q(x)$, this principle must be modified slightly. It can be shown that the solution of eq. (4) is a local minimum wherever $q'(G) > 0$ and a local maximum wherever $q'(G) < 0$. It follows that the decreasing part of the S-shaped curve is an unstable equilibrium point.

In this section, we thus assume that this minimization principle is valid, and show that it allows to uniquely define the pressure distribution and the flow rate of the plateau.

In the Poiseuille configuration, all positions along the x-axis should have the same flow rate. Therefore, no more than two pressure gradients are admissible, denoted as G_1 and G_2, which need to be determined. Figure 5 illustrates a potential streamwise banding configuration. We can also define l as the total length with the gradient G_1, and thus $L - l$ represents the total length with gradient G_2. The solution is then determined by three unknown variables G_1, G_2, and l, with the constraint $\Delta P = \int_0^L G dx = lG_1 + (L - l)G_2$.

The minimization of the functional eq. (5) can thus be found using the Lagrangian multiplier (λ here) method:

$$(G_1, G_2, l, \lambda) = \arg\max_{\lambda} \min_{l,G_1,G_2} \left[l\varphi(G_1) + (L - l)\varphi(G_2)\right] - \lambda(lG_1 + (L - l)G_2 - \Delta P)]$$

It follows the three equalities:

$$\lambda = \frac{\varphi(G_1) - \varphi(G_2)}{G_1 - G_2} = \varphi'(G_1) = \varphi'(G_2) \hat{=} \hat{q} \tag{7}$$

and

$$l = \frac{\Delta P - LG_2}{G_1 - G_2}. \tag{8}$$

Unsurprisingly, the solution is very similar to spinodal decomposition, where two phases can coexist only for an average pressure drop $\Delta P/L$ between two specific pressure gradients G_1 and G_2 that satisfy equation (7), and the flow rate is imposed by $\hat{q} = \varphi'(G_1) = \varphi'(G_2)$. The proportion of each phase follows the Maxwell construction rule eq. (8). It is worth mentioning that in this system, each x locations are almost independent and related only by the total flow rate. Moreover, every positions are interchangeable, one cannot predict where each phase are located, only their total length.

From the function $\phi(y)$, the two values G_1 and G_2 and $\hat{q}$ can be determined using the chord method or the Legendre transform. An example of the relationship between flow rate - pressure drop is illustrated in Figure 6 for a concentration of $\phi = 0.425$. If this approach indeed predicts a long plateau with a constant flow rate, it fails to capture the non-monotonic "bump" observed experimentally. The reason behind this may lie in the fact that this solution is a global minimum of the functional, while any solution for which $q'(G) > 0$ for all x, is a local minimum of the total energy. Once such solution is reached, one would thus need to overcome energy barriers to reach the global minimum, with thermal energy fluctuations for instance.

B. Dynamical model

In the absence of thermal fluctuations, the final solution will be the first stable one reached. Therefore, it is important to describe the time evolution of the flow leading to a non-monotonic Poiseuille flow. To illustrate this, we can write a simple dynamical model whose steady state exhibits an S-shaped relationship between flow rate and pressure gradient. For this purpose, we introduce a dynamical stochastic version of the Wyart-Cates rheological model, inspired by the model introduced by [21].

Here, we simply assume that the total number of bonds is fixed and that the probability per unit of time (frequency) to create a "frictional" bond from a "frictionless" one is proportional to the applied stress with certain characteristic frequency. On another hand, "frictional" contacts can be destroyed and become "friction-

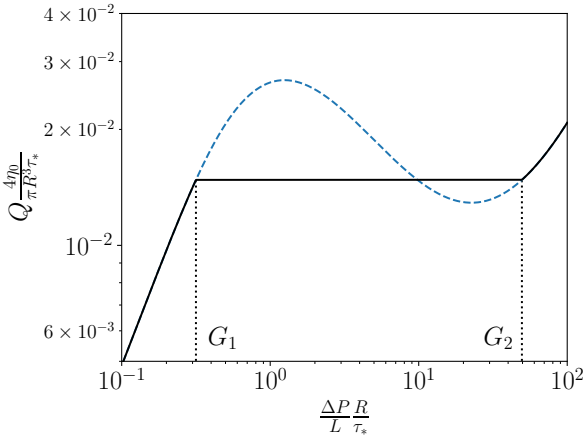

Figure 6. Flow curve as a function of the mean pressure gradient $\Delta P/L$ for a fluid with S-shaped rheology according to the minimum dissipation principle. The flow rate follows the RW equation until it reaches the pressure gradient G_1 and a flow rate $\hat{q}$. Between the gradients G_1 and G_2, the system segregates between regions with gradient G_1 and regions with gradient G_2 following the Maxwell construction (see sketch in Figure 5)

less" one with another frequency.

The second approximation we make is to assume that the fraction of "frictional" contacts and thus the viscosity is homogeneous in the gap, which then allows to identify the flow rate to the shear rate, and the stress to an average pressure gradient. This approximation is similar to neglecting the n term in the WR equation eq. (1).

This allows to write a dynamical equation for f in the form:

$$\frac{df(x)}{dt} = \frac{1}{t_1}\frac{G}{G_*}(1-f(x)) - \frac{1}{t_2}f(x), \tag{9}$$

where G_* is a characteristic pressure gradient that characterizes the typical stress for making "frictional" contact. t_1 and t_2 are characteristic times (the inverse frequency) for frictional contact formation and destruction, respectively. In principle, these two times are expected to be inversely proportional to the shear rate, so they are parameterized as $t_1 = \delta_1/q$, $t_2 = \delta_2/q$. This requires the use of a variable time step in the numerical scheme described later. Note, however, that q is the same for each x, so one could have fixed these two times without changing the final state.

We also note that the equilibrium state of equation eq. (9) is:

$$f_{eq} = \frac{G/G_*}{t_1/t_2 + G/G_*}, \tag{10}$$

which is slightly different from the exponential relationship proposed by Wyart and Cates [10] or the one by Mari *et al.*[9]. An alternative approach could be to impose the equilibrium state in the dynamic equation [30, 31], but this would lead to the loss of the simple phenomenological description of eq. (9).

The averaged viscosity is then a function of f according to eq. (2). For the sake of simplicity, we use η_r and η_s as parameters instead of ϕ. The simulation consists of the following steps. First, we initialize the f field by randomly drawing according to a uniform distribution with mean f_0 and standard deviation σ_f. The pressure field is then calculated using eq. (4), which with the above hypothesis leads to $Q = \frac{\pi R^4}{8\eta(f)}G(x)$, with the viscosity field derived from eq. (2) and imposing the total pressure drop $\Delta P = \int_0^L G dx$. From the pressure gradient field, the f field is then updated using eq.(9) to advance in time. The procedure is then repeated until the flow rate converges. Note that in this system of equation, we neglect the advection assuming that the relaxation time is shorter than the advection time. In principle, the f field should be advected with q.

For the numerical parameters, the number of discretization points is 201, the characteristic pressure gradient is $G_* = 10$, and $\delta_1 = \delta_2$, the time step is variable such that $dt = 1e^{-4}\delta_1/q$.

This system of equations corresponds to a dynamical system with three equilibrium points for each x location: two stable and one unstable (from an energy point of view). Interestingly, each dynamical system is linked by the constraint $\Delta P = \int_0^L G dx$. For example, if a region has a higher viscosity, the pressure gradient will be higher, which will reduce the pressure gradient (and thus the stress) in other regions, and vice versa.

Figure 7 [left] illustrates this dynamic behavior. In this figure, we plot the time evolution of the pressure gradient $\partial_x P = G$, as function of the flow rate Q for each location. Note that the flow rate is the same at each location at each time. So the intersection with any horizontal line corresponds to all states at a given time. Here we initialize the system with a mean value of $f_0 = 0.5$ and $\sigma_f = 0.2$. For this pressure drop and initial conditions, the total flow rate initially decreases as f (and hence the viscosity) increases for each location. However, we see that the G distribution becomes broader in this case. This is because the viscosity increase is greater at some locations than at others: it will thus raise the pressure gradient at these locations, but lower it at others.

As a result, the trajectories separate and some locations converge to the high-gradient stable solution, G_+, while others converge to the low-gradient solution, G_-. Interestingly, some locations initially seem to converge to the high gradient solution, but then turn back to the other.

From this figure we can see how important the initial state is, as it is the highest initial value of f that will reach the highest gradient solution and force the other locations to reach the other stable point. This is also illustrated in Figure 7 (right), where we choose a very homogeneous initial state (low σ_f). All locations are therefore almost identical and follow the same trajec-

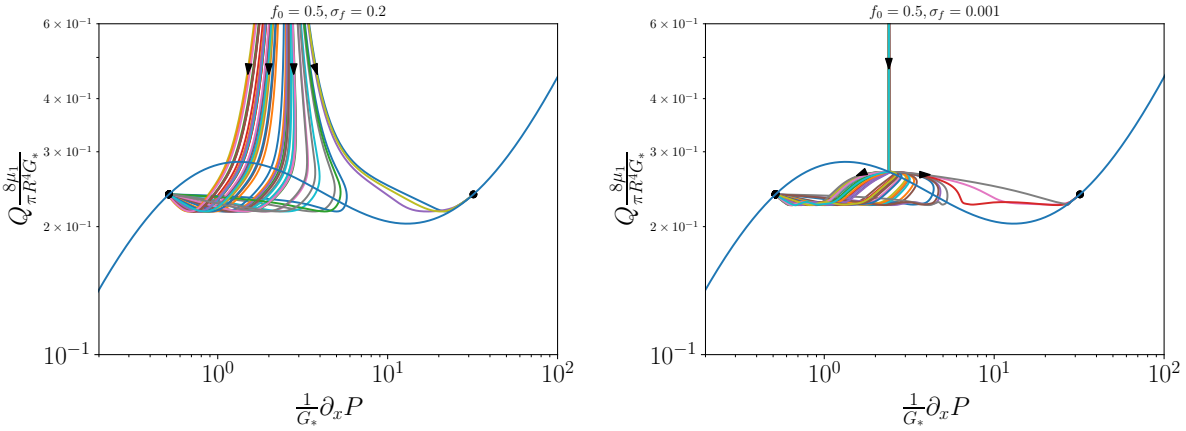

Figure 7. Temporal evolution of the system for two different initial conditions. Each x-location is represented by a trajectory $(Q(t), \partial_x P(t))$. Initially, the flow rate is high. The dispersion of the pressure gradient is a consequence of the initial distribution of f (and thus of the viscosity). With time, the flow rate decreases and the different pressure gradients diverge. Some locations converge to a low gradient in the $q(G)$ curve, while others converge to a higher pressure gradient. Left: The initial distribution is quite heterogeneous $f_0 = 0.5$ and $\sigma_f = 0.2$. Right: The initial distribution is much more homogeneous ($f_0 = 0.5$ and $\sigma_f = 0.01$), with $\eta_r/\eta_s = 300$. In the latter case, all the trajectories are similar until the function $q(G)$ is reached, at which point they start to diverge.

tory. The viscosity thus decreases homogeneously until the trajectories reach the unstable equilibrium point. Since this state is unstable, all trajectories eventually diverge from it and move towards one of the two stable solutions. Again, we see that some points make a U-turn when other locations reach very high viscosity values. Another observation is that the final flow rates for these two cases are quite close, although the time evolution is significantly different. This figure shows that there are two stable states (low G_- and high G_+ gradient states) and an intermediate unstable state. Furthermore, in Appendix B and Figure 10 we report initial conditions where all trajectories converge to either the low gradient state (left), the high gradient state (right) or both (middle).

Figure 8 (left) shows the final flow rate Q_f averaged over ten different initial conditions as a function of the applied pressure drop. For a low value of $\Delta P/L$, Q follows the function $q(G)$ as expected (as shown on the left of Figure 10). After reaching the local maximum of $q(G)$, the flow drops abruptly to a lower value. The flow rate then no longer follows $q(G)$ but a very slowly decreasing plateau. This plateau corresponds to the streamwise phase banding sketched in Figure 5 and is likely to account for the maximum-jump-plateau observed in the experiments. This can be quantified by measuring the relative length of the high gradient regions: $1 - l/L$ as shown in Figure 8 (right). The total length of the high viscous band is thus increasing with the pressure drop[37]. We also note that the flow value is relatively close to the minimum energy dissipation (horizontal dashed line), although $G_- \neq G_1$ and $G_+ \neq G_2$. However, the flow curve in the banding region appears to be relatively sensitive to the initial conditions. As shown in Figure 8, it is sensitive to the mean value of the fraction of frictional contact f_0. But this sensitivity is much stronger with the homogeneity of the initial condition, as shown in Figure 9. For a low value of σ_f, the plateau decays slowly to the local minimum of $q(G)$. For a higher value of σ_f ($\gtrsim 0.2$) the banding transition occurs before the local maximum of $q(G)$ is reached. A constant value is then observed for a range of pressure drops, but the flow rate starts to increase at an intermediate pressure drop before reaching the high viscosity stable branch. We conclude that the initial state, namely the pre-stress, but also its homogeneity, can have a significant influence on the banding regime. This is confirmed in Appendix B (Figure 10), which shows that by choosing the initial conditions, all trajectories can converge to either the low gradient state (left), i.e. the homogeneous gradient ($l = L$) monotonic part of the curve up to its maximum (CST), the high gradient homogeneous state ($l = 0$, right), or the streamwise banding state ($0 < l < L$, middle).

V. DISCUSSION AND CONCLUSION

In this work, we have used the Poiseuille capillary flow configuration to assess the S-shape rheology of corn starch solution. The advantage of this geometry is that it is likely to prevent vorticity banding, which has been reported in the literature to explain the difficulty in observing the S-shape flow curve in a classical rheometer. Experimentally, we have observed that the flow rate as a function of pressure drop is indeed non-monotonic, which could confirm an S-shaped rheology. However, the curve does not follow the shape expected from the classical Wyart and Cates model. As the pressure drop increases, the flow rate first increases monotonically up

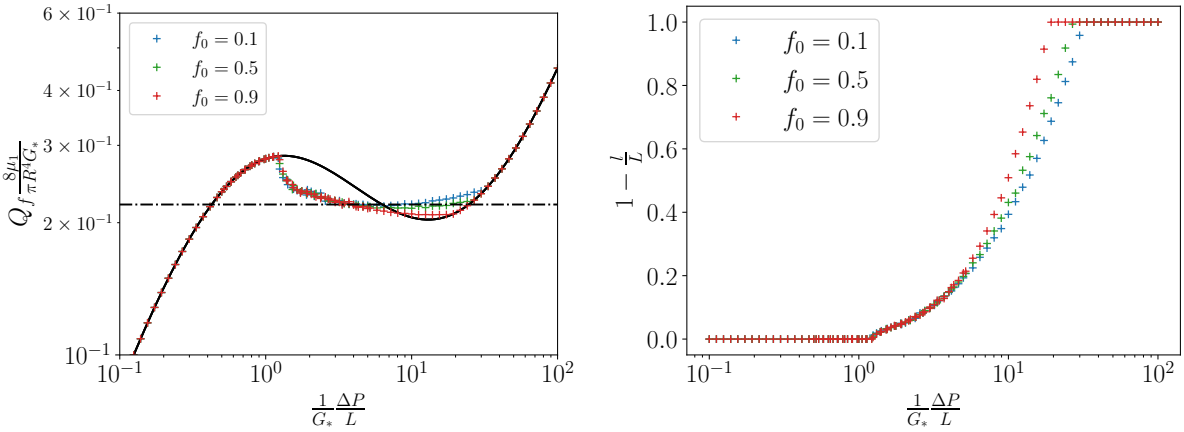

Figure 8. Left: Flow rate versus applied pressure drop obtained from the model, different colors represent different initial mean values of the number of frictional contacts, f_0, with $\sigma_f = 0.1$. The black curve represents the curve $q(\partial_x P)$. Right: For the corresponding simulation, fraction of the region of high pressure gradient G_+ as a function of the applied pressure drop.

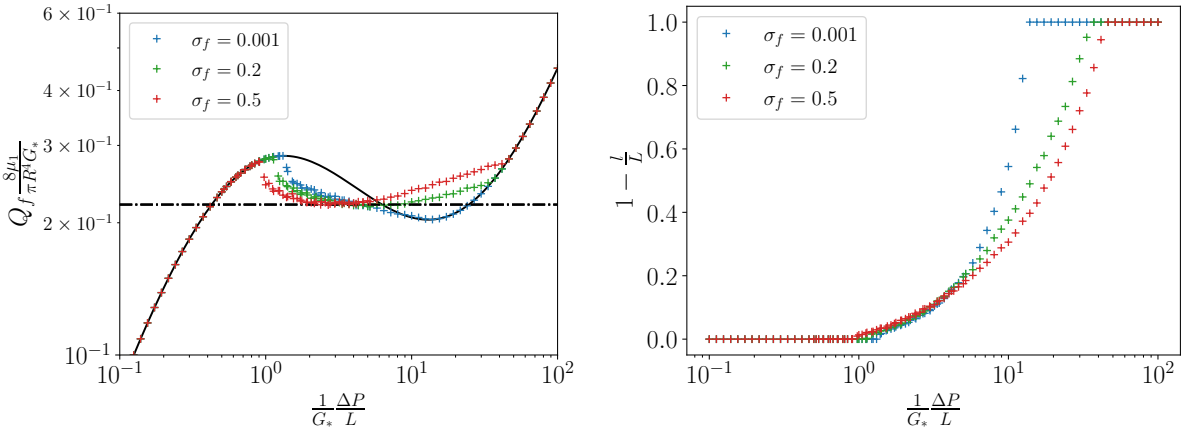

Figure 9. Left: Flow rate versus applied pressure drop obtained from the model, different colors represent different heterogeneity of the initial distribution of frictional contact, σ_f, with $f_0 = 0.5$. The black curve represents the curve $q(\partial_x P)$. Right: For the corresponding simulation, fraction of the region of high pressure gradient G_+.

to a maximum, where the flow rate drops abruptly, and then remains almost constant over a wide range of pressure drops. To account for this discrepancy, we note that in our flow configuration, it is the total pressure drop that is imposed, not the local pressure gradient. This allows us to address solutions where the pressure gradient is not homogeneous in the flow direction. The flow would then be structured in bands in the flow direction: streamwise banding.

A natural idea to address this problem is to make an analogy to spinodal decomposition. For the non-monotonic flow rate versus the local pressure gradient, we assume that the solution minimizes the viscous dissipation, then phase separation can be expected. Each phase corresponds to a different viscosity and pressure gradient. This approach leads to an increase followed by a plateau, but no decrease at all. While this method correctly predicts a plateau in flow rate, it cannot explain the abrupt drop beyond a maximum. The failure of this approach may be due to the presence of many local minima in the energy function.

Since the chosen solution is not necessarily the minimal one, we propose a simple dynamic model based on the Wyart and Cates viscosity model, which is able to reproduce an S-shaped relationship between the flow rate and the local pressure gradient. As a result, this model indeed shows the existence of a phase separation between high and low viscosity regions. As the total pressure drop increases, the flow rate first increases, then suddenly decreases, and then remains almost constant until it increases again. This evolution of the flow rate with total pressure drop is quite similar to the experimental one, supporting the validity of the streamwise banding hypothesis. In the experiment we don't observe an increase at high pressure drop, this is most likely due to a not large enough range for the pressure (note on Figure 2 the wide range of pressure required). Furthermore our model shows that this plateau region

is relatively dependent on the initial state of the fluid. This can be understood from the fact that each location is connected by the imposed total pressure difference. The first region to reach very high viscosity causes a drop in the pressure gradient in the other regions. Similarly, we have also implemented different dynamical model eq. (9) leading to a different equilibrium function for the fraction of frictional contacts (see [10, 30]). It follows that the model does not affect the qualitative shape of the flow curve, but only the height of the plateau.

We can now discuss some aspect of our results. First, it is important to emphasize that our approach is based on several assumptions. The Weißenberg-Rabinowitsch relation is based on the lubrication approximation, which assumes that the pressure gradient is oriented along the flow direction. We also assume that the suspension remains homogeneous in the gap, which precludes, for example, shear-induced migration [38]. Finally, we assume that the Wyart and Cates model is valid, or at least an S-shaped rheology. All these hypotheses are difficult to verify at the present time. But the main result of this paper is to show that if there is a non-montonic relationship between the flow rate and the local pressure gradient, another type of banding than "shear banding" or "vorticity banding" can be expected: "streamwise banding".

As discussed in the introduction, Bougouin *et al.* [29] observed recently a frictional soliton propagating upward. This observation could probably be related to the streamwise banding. However, the interpretation of this phenomena differ significantly. The authors invoke the dilatation, permeation and the concentration inhomoeneity. Our conclusion of the present paper is that the only presence of a non-monotonic rheological curve is sufficient to predict the occurence of stress banding in the streamwise direction, even if the suspension remains homogeneous. This is because the decreasing part of the Poiseuille flow curve is likely to be mechanically unstable. We note that our model is unable to predict any upstream propagation of these bands.

In the model used, all field values are interchangeable in position. Therefore, it cannot predict anything about the position, number and extension of the bands (Figure 5). To do so, one could for instance introduce spatial derivative terms. For example, extending the analogy with a phase transition, one could introduce a gradient penalizing term in the energy functional as suggested by Cahn and Hilliard [33]. This could potentially lead to a frontal propagation velocity, but also to a solution selection criterion (see [18] and references therein for shear banding). However, without knowing more about the physical phenomena involved, it is difficult to go further.

It is also interesting to note that the approach used here is quite analogous to the shear banding approach proposed by Spenley *et al.*[39] when the function $\dot{\gamma}(\tau)$ is non-monotonic. In this case, one can also expect a spinodal decomposition, but for the shear rate instead of the pressure gradient.

Another hypothesis in our model is that we discard advection. Since the flow is very slow, we assume that the time rate of evolution for f is small enough compared to advection. But one could expect that the f field (and thus the bands) could propagate with the flow. To improve the model, one could then translate the f field along the x direction, introducing fluid with a new "fresh" f distribution at the inlet and ejecting some older fluid at the outlet. It would be interesting to observe how the new fluid and the ejected fluid affect by the rest of the fluid that has already converged to a stable gradient.

Finally, a final comment can be made about the rheometry of such a fluid using a cylinder or cone-plate configuration. In this case, axisymmetry prevents vorticity banding, which is replaced by streamwise banding. This occurs because we do not impose the pressure gradient, but the total pressure drop, allowing the pressure gradient to segregate. However, it could be argued that a similar phenomenon could occur in a rheometer, since it is a total force (or torque) that is applied, not a local stress. Similar stress segregation in the flow direction cannot be excluded.

Future work will be devoted to characterize the experimental results. In particular, we want to analyze the flow in more detail in order to detect any streamwise banding.

AUTHOR CONTRIBUTION STATEMENT

LT and DS did the experimental measurements, physical analysis, and writing. LT performed the numerical simulations.

DATA AVAILABILITY STATEMENT

Data sets generated during the current study are available from the corresponding author on reasonable request.

ACKNOWLEDGEMENTS

The authors thanks B. Darbois-Texier, G. Gauthier for fruitfull discussions.

[1] A. Fall, A. Lemaitre, F. Bertrand, D. Bonn, and G. Ovarlez, "Continuous and discontinuous shear thickening in granular suspension," Phys. Rev. Lett **105**,

268303 (2010).

[2] A. Fall, F. Bertrand, D. Hautemayou, C. Mezière, P. Moucheront, A. Lemaître, and G. Ovarlez, "Macroscopic discontinuous shear thickening versus local shear jamming in cornstarch," Phys. Rev. Lett. **114**, 098301 (2015).

[3] M. M. Denn, J. F. Morris, and D. Bonn, "Shear thickening in concentrated suspensions of smooth spheres in newtonian suspending fluids," Soft Matter **14**, 170–184 (2018).

[4] E. Brown and H. M. Jaeger, "Shear thickening in concentrated suspensions: phenomenology, mechanisms and relations to jamming," Reports on Progress in Physics **77**, 046602 (2014).

[5] A. Gauthier, G. Ovarlez, and A. Colin, "Shear thickening in presence of adhesive contact forces: The singularity of cornstarch," Journal of Colloid and Interface Science **650**, 1105–1112 (2023).

[6] A. Fall, F. Bertrand, G. Ovarlez, and D. Bonn, "Shear thickening of cornstarch suspensions," Journal of rheology **56**, 575–591 (2012).

[7] H. Nakanishi, S. Nagahiro, and N. Mitarai, "Fluid dynamics of dilatant fluids," Phys. Rev. E **85**, 011401 (2012).

[8] J. F. Brady and G. Bossis, "The rheology of concentrated suspensions of spheres in simple shear flow by numerical simulation," Journal of Fluid Mechanics **155**, 105–129 (1985).

[9] R. Mari, R. Seto, J. F. Morris, and M. M. Denn, "Shear thickening, frictionless and frictional rheologies in non-Brownian suspensions," Journal of Rheology **58**, 1693–1724 (2014), https://pubs.aip.org/sor/jor/article-pdf/58/6/1693/15612580/1693_1_online.pdf.

[10] M. Wyart and M. E. Cates, "Discontinuous shear thickening without inertia in dense non-brownian suspensions," Phys. Rev. Lett. **112**, 098302 (2014).

[11] C. Clavaud, A. Bérut, B. Metzger, and Y. Forterre, "Revealing the frictional transition in shear-thickening suspensions," Proceedings of the National Academy of Sciences **114**, 5147–5152 (2017), https://www.pnas.org/doi/pdf/10.1073/pnas.1703926114.

[12] É. Guazzelli and O. Pouliquen, "Rheology of dense granular suspensions," Journal of Fluid Mechanics **852**, P1 (2018).

[13] Z. Pan, H. de Cagny, B. Weber, and D. Bonn, "S-shaped flow curves of shear thickening suspensions: Direct observation of frictional rheology," Phys. Rev. E **92**, 032202 (2015).

[14] R. Mari, R. Seto, J. F. Morris, and M. M. Denn, "Nonmonotonic flow curves of shear thickening suspensions," Physical Review E **91**, 052302 (2015).

[15] J. F. Morris, "Shear thickening of concentrated suspensions: Recent developments and relation to other phenomena," Annual Review of Fluid Mechanics **52**, 121–144 (2020).

[16] B. Darbois Texier, H. Lhuissier, Y. Forterre, and B. Metzger, "Surface-wave instability without inertia in shear-thickening suspensions," Communications Physics **3**, 232 (2020).

[17] G. M. H. Wilkins and P. D. Olmsted, "Vorticity banding during the lamellar-to-onion transition in a lyotropic surfactant solution in shear flow," The European Physical Journal E **21**, 133–143 (2006).

[18] P. D. Olmsted, "Perspectives on shear banding in complex fluids," Rheologica Acta **47**, 283–300 (2008).

[19] G. Ovarlez, S. Rodts, X. Chateau, and P. Coussot, "Phenomenology and physical origin of shear localization and shear banding in complex fluids," Rheologica Acta **48**, 831–844 (2009).

[20] A. Fall, F. Bertrand, G. Ovarlez, and D. Bonn, "Yield stress and shear banding in granular suspensions," Phys. Rev. Lett. **103**, 178301 (2009).

[21] R. N. Chacko, R. Mari, M. E. Cates, and S. M. Fielding, "Dynamic vorticity banding in discontinuously shear thickening suspensions," Phys. Rev. Lett. **121**, 108003 (2018).

[22] M. Hermes, B. M. Guy, W. C. K. Poon, G. Poy, M. E. Cates, and M. Wyart, "Unsteady flow and particle migration in dense, non-Brownian suspensions," Journal of Rheology **60**, 905–916 (2016), https://pubs.aip.org/sor/jor/article-pdf/60/5/905/16729455/905_1_online.pdf.

[23] F. M. Rocha, Y. Forterre, B. Metzger, and H. Lhuissier, "Drag of a shear-thickening suspension on a rotating cylinder," Journal of Fluid Mechanics **970**, A35 (2023).

[24] B. Saint-Michel, T. Gibaud, and S. Manneville, "Uncovering instabilities in the spatiotemporal dynamics of a shear-thickening cornstarch suspension," Phys. Rev. X **8**, 031006 (2018).

[25] G. Chatté, J. Comtet, A. Nigues, L. Bocquet, A. Siria, G. Ducouret, F. Lequeux, N. Lenoir, G. Ovarlez, and A. Colin, "Shear thinning in non-brownian suspensions," Soft matter **14**, 879–893 (2018).

[26] B. Rabinowitsch, "Über die viskosität und elastizität von solen," Zeitschrift für Physikalische Chemie **145A**, 1 – 26 (1929).

[27] L. Isa, R. Besseling, A. N. Morozov, and W. C. K. Poon, "Velocity oscillations in microfluidic flows of concentrated colloidal suspensions," Phys. Rev. Lett. **102**, 058302 (2009).

[28] P. Kanehl and H. Stark, "Self-organized velocity pulses of dense colloidal suspensions in microchannel flow," Phys. Rev. Lett. **119**, 018002 (2017).

[29] A. Bougouin, B. Metzger, Y. Forterre, P. Boustingorry, and H. Lhuissier, "A frictional soliton controls the resistance law of shear-thickening suspensions in pipes," Proceedings of the National Academy of Sciences **121**, e2321581121 (2024), https://www.pnas.org/doi/pdf/10.1073/pnas.2321581121.

[30] A. Singh, R. Mari, M. M. Denn, and J. F. Morris, "A constitutive model for simple shear of dense frictional suspensions," Journal of Rheology **62**, 457–468 (2018).

[31] J. A. Richards, J. R. Royer, B. Liebchen, B. M. Guy, and W. C. K. Poon, "Competing timescales lead to oscillations in shear-thickening suspensions," Phys. Rev. Lett. **123**, 038004 (2019).

[32] We also tried using our own rheometer. Similar to the literature [22], we observed a monotonic DST curve, but with shear rate fluctuating significantly.

[33] J. W. Cahn and J. E. Hilliard, "Free Energy of a Nonuniform System. I. Interfacial Free Energy," The Journal of Chemical Physics **28**, 258–267 (1958), https://pubs.aip.org/aip/jcp/article-pdf/28/2/258/18813541/258_1_online.pdf.

[34] D.J. Korteweg, "Xvii. on a general theorem of the stability of the motion of a viscous fluid," The London, Edinburgh, and Dublin Philosophical Mag-

azine and Journal of Science **16**, 112–118 (1883), https://doi.org/10.1080/14786448308627405.
[35] R. B. Bird, "New variational principle for incompressible non-newtonian flow," Phys. Fluids **3**, 539–541 (1960), https://aip.scitation.org/doi/pdf/10.1063/1.1706087.
[36] L. Talon, "Minimum principle for the flow of inelastic non-newtonian fluids in macroscopic heterogeneous porous media," Phys. Rev. Fluids **7**, L042101 (2022).
[37] Although it is difficult to see it on a semilog plot, this increase is almost linear. At least at the beginning of the "plateau.".
[38] D. Leighton and A. Acrivos, "The shear-induced migration of particles in concentrated suspensions," Journal of Fluid Mechanics Digital Archive **181**, 415–439 (1987).
[39] N. Spenley, X. Yuan, and M. Cates, "Nonmonotonic Constitutive Laws and the Formation of Shear-Banded Flows," Journal de Physique II **6**, 551–571 (1996).

Appendix A: Imposing the flow rate

A complementary measurement can be obtained by measuring the pressure drop at a given flow rate $\Delta P(Q)$ in our capillary rheometer. To do this, we control the flow rate Q with a constant flow syringe pump (NEMESYS syringe) and measure the inlet pressure leading to $\Delta P(Q)$. The green square in Figure 11, is a plot of ΔP versus the controlled flow rate Q of the syringe, using $\tau = \Delta PR/(2L)$ on the vertical axis. As the flow rate is increased from low values, the pressure drop, i.e. τ, increases monotonically up to a flow rate value at which the pressure increases drastically to the maximum measurable with our instrument while the flow rate remains constant. To reduce the pressure drop, we need to reduce the flow rate. Therefore, in this flow rate controlled experiment, we get a $\Delta P(Q)$ curve that is monotonic up to a maximum flow rate Q_M at which the pressure increases almost without limit. For comparison at the same concentration, on Figure 11, we plot the values obtained in two experiments using the pressure controlled device leading to $Q(\tau)$: the data obtained by the two devices are clearly consistent in the monotonic part up to the maximum-jump value Q_M. Hence with the syringe, we can just access to the continuous shear thickening part of the curve and are unable to access the jump-plateau part of the flow curve. This behaviour is reminiscent of the one observed in spherical particles suspensions [13] but with neither hysteresis effects nor instabilities. Indeed such a jump-plateau, to our knowledge, has not been reported in the literature : in the case of Couette cylindrical geometry or controlled shear rate [23] a discontinuous vertical shear thickening is barely observed whereas controlled shear stress controlled shear rate [16, 22, 24] show almost S-shape but with instabilities.

Appendix B: Example of the model trajectories

In Figure 10, we show that choosing different initial conditions, all the trajectories can converge either to the low-gradient state (left), that is the homogeneous gradient monotonic ($l = L$) part of the curve up to its maximum, the high-gradient homogeneous state ($l = 0$, right) and the streamwise banding heterogeneous state ($0 < l < L$, middle).

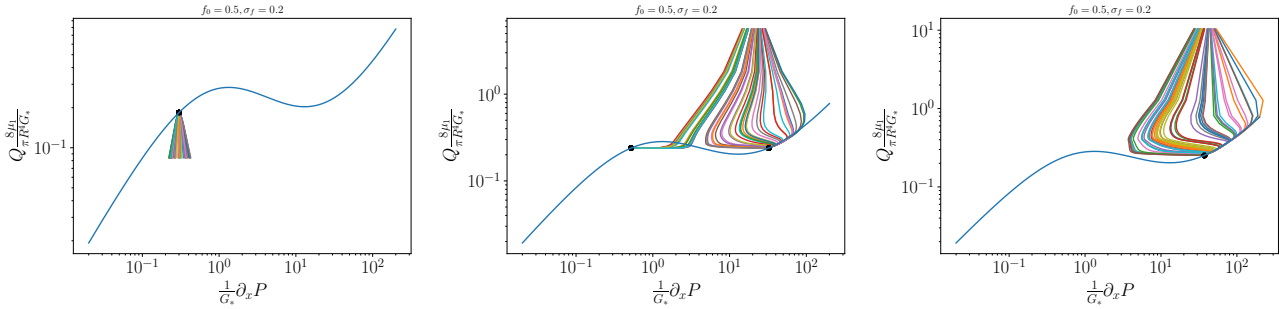

Figure 10. By choosing the initial conditions, all trajectories can converge to either the low homogeneous state (left), the high gradient homogeneous state (right), or the streamwise banding state (middle).

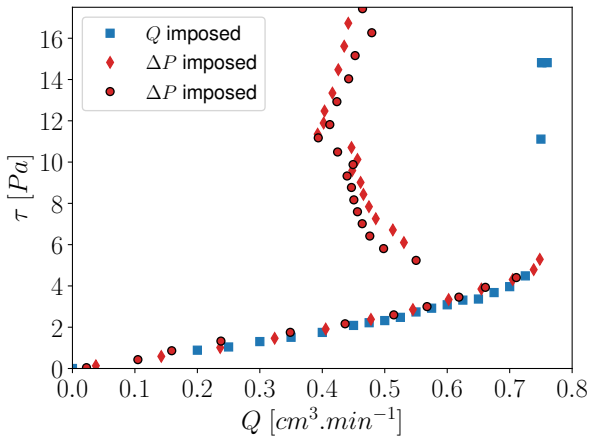

Figure 11. Comparison between experiments at controlled flow rate Q leading to $\Delta P(Q)$ and hence to $\tau(Q)$ (green square) with the curves $\tau(Q)$ obtained from two experiments at controlled pressure (red circles and diamonds). Concentration of the three experiments : $\phi = 40\ \%$